Bio-Design and Manufacturing (2026) 9:80–93
https://doi.org/10.1631/bdm.2500119

RESEARCH ARTICLE

Precision organoid segmentation technique (POST): accurate organoid segmentation in challenging bright-field images

Xuan Du[1,2] · Yuchen Li[2] · Jiaping Song[4] · Zilin Zhang[1] · Jing Zhang[2] · Yanhui Li[3] · Zaozao Chen[1,2] · Zhongze Gu[1]

Received: 16 March 2025 / Accepted: 28 July 2025 / Published online: 27 December 2025

Abstract

Organoids possess immense potential for unraveling the intricate functions of human tissues and facilitating preclinical disease treatment. Their applications span from high-throughput drug screening to the modeling of complex diseases, with some even achieving clinical translation. Changes in the overall size, shape, boundary, and other morphological features of organoids provide a noninvasive method for assessing organoid drug sensitivity. However, the precise segmentation of organoids in bright-field microscopy images is made difficult by the complexity of the organoid morphology and interference, including overlapping organoids, bubbles, dust particles, and cell fragments. This paper introduces the precision organoid segmentation technique (POST), which is a deep-learning algorithm for segmenting challenging organoids under simple bright-field imaging conditions. Unlike existing methods, POST accurately segments each organoid and eliminates various artifacts encountered during organoid culturing and imaging. Furthermore, it is sensitive to and aligns with measurements of organoid activity in drug sensitivity experiments. POST is expected to be a valuable tool for drug screening using organoids owing to its capability of automatically and rapidly eliminating interfering substances and thereby streamlining the organoid analysis and drug screening process.

Graphical abstract

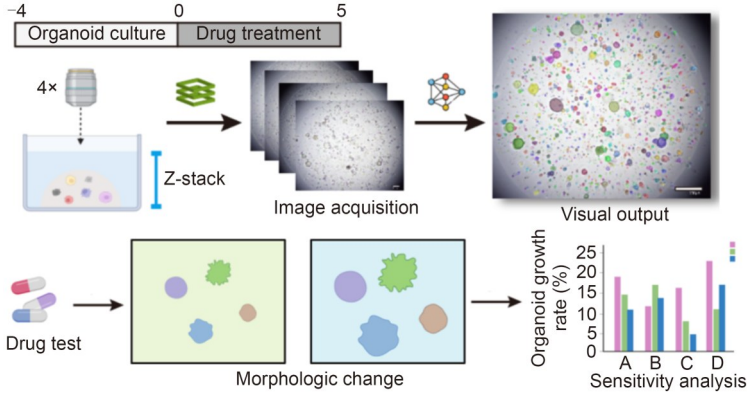

Keywords Organoid · Drug screening · Deep learning · Image segmentation

✉ Yanhui Li
yanhuili@nju.edu.cn

✉ Zaozao Chen
101012282@seu.edu.cn

✉ Zhongze Gu
Gu@seu.edu.cn

[1] State Key Laboratory of Digital Medical Engineering, School of Biological Science and Medical Engineering, Southeast University, Nanjing 211189, China

[2] Jiangsu Avatarget Biotechnology Co., Ltd., Nanjing 215163, China

[3] State Key Laboratory for Novel Software Technology, Nanjing University, Nanjing 210008, China

[4] Anhui Province Key Laboratory of Functional Agriculture and Functional Food, Anhui Science and Technology University, Chuzhou 239200, China

1 Introduction

Because of their ability to mimic certain organs in structure and physiological function, organoids hold great potential for understanding the complex functions of human tissues and facilitating preclinical disease treatment [1, 2]. Applications range from high-throughput drug screening to complex disease modeling, with some even reaching clinical translation. Specifically, organoids have been used to simulate complex tumor microenvironments to improve understanding of cancer biology [3]. They can also serve as a platform for drug discovery by enabling researchers to assess the efficacy and toxicity of new therapeutic drugs [4]. However, current methods for evaluating organoid drug sensitivity still have several limitations. Cell viability assays, such as those based on adenosine triphosphate (ATP) and cell counting kit-8 (CCK-8), are considered the gold standard for assessing organoid drug sensitivity [5]. ATP-based assays measure cell metabolism by quantifying the ATP level, which reflects the number of live cells. They require cell membrane lysis to release ATP, which results in cell death and limits the assessment to a single time point. Consequently, they cannot evaluate changes in cell viability over time, particularly before and after drug treatment [6]. Furthermore, organoid systems typically comprise diverse cell types with an extracellular matrix, secretions, cell-to-cell interactions, and dynamic changes in cellular states and the external environment. These complex components and variations can further interfere with the precise measurement of ATP in organoid cultures [7, 8].

Morphological changes in the size, shape, boundary, and topological structure of an organoid are the most intuitive and effective indicators of its response to normal or drug-induced conditions. The morphology reflects the organoid phenotype and can be conveniently and quickly observed by bright-field microscopy. However, analysis of bright-field microscopy images is more difficult than that of confocal-based fluorescence images because of the limited information provided—unless complex processing techniques such as layered scanning and thresholds for filtering the background are applied—as well as possible environmental fluctuations. In recent years, deep learning has become increasingly important for organoid analysis because it greatly improves the efficiency and accuracy of drug screening, disease modeling, personalized treatment, and clinical diagnosis [9–11]. In particular, the segmentation of organoids in bright-field images has become a research hotspot [12]. Gritti et al. [13] introduced MOrgAna, which utilizes logistic regression and a multilayer perceptron for organoid segmentation. However, their method has difficulty in capturing spatial information and lacks a strong nonlinear fitting capability when dealing with complex morphologies. Powell et al. [14] proposed deepOrganoid, which is a cell viability model for matrix-embedded organoids based on bright-field imaging, but it is only suitable for simple imaging backgrounds. Matthews et al. [15] introduced OrganoID while Wang et al. [16] proposed RDAU-Net; both are based on the U-Net architecture, which focuses on pixel-level classification. However, these models do not provide organoid instance segmentation and perform poorly in organoid overlap or occlusion cases. Lefferts et al. [17] developed OrgaSegment for instance segmentation and applied it to quantify cystic fibrosis transmembrane conductance regulator (CFTR)-dependent fluid secretion. However, their method is based on Mask region-based convolutional neural network (R-CNN), which may produce excessive detections when handling dense or overlapping targets and result in false positives or unclear segmentation. Additionally, OrgaSegment is prone to missing smaller organoids and failing to capture fine details accurately when applied to segmenting complex morphologies or organoids with indistinct boundaries (Fig. S1 in the supplementary information).

Although various deep-learning algorithms have been applied to organoid image analysis [6, 9, 10, 12, 18, 19], there is no universal and accurate algorithm to reliably analyze bright-field images for organoid-based drug screening owing to the complexity of organoid morphologies [12]. The emergence of pretrained prompt models for image segmentation such as the segmentation anything model (SAM) [20] is promising, but their application in specialized fields such as for cell or organoid segmentation tasks remains limited because of inadequate generalization [21, 22]. In this study, we developed the precision organoid segmentation technique (POST), which is an accurate algorithm for organoid segmentation of bright-field microscopy images. Unlike existing methods, POST not only ensures the precise segmentation of each organoid and the accurate extraction of its morphological data but also effectively addresses various challenges associated with imaging artifacts and culture conditions in high-resolution bright-field images. POST allows for both automatic and semiautomatic segmentation of various organoids under bright-field conditions by distinguishing individual organoids using different colors (Fig. 1). We applied POST to three-dimensional (3D) organoids and demonstrated a high correlation between organoid morphological characteristics and viability. Thus, it is expected to be an effective and reliable tool for drug prescreening under conventional or simple imaging conditions as well as a valuable complement for cell viability assessments in more challenging scenarios.

2 Results

2.1 Model design

POST (Fig. 2a) incorporates the zero-shot generalization, flexible prompts, and large-scale pretraining of SAM to

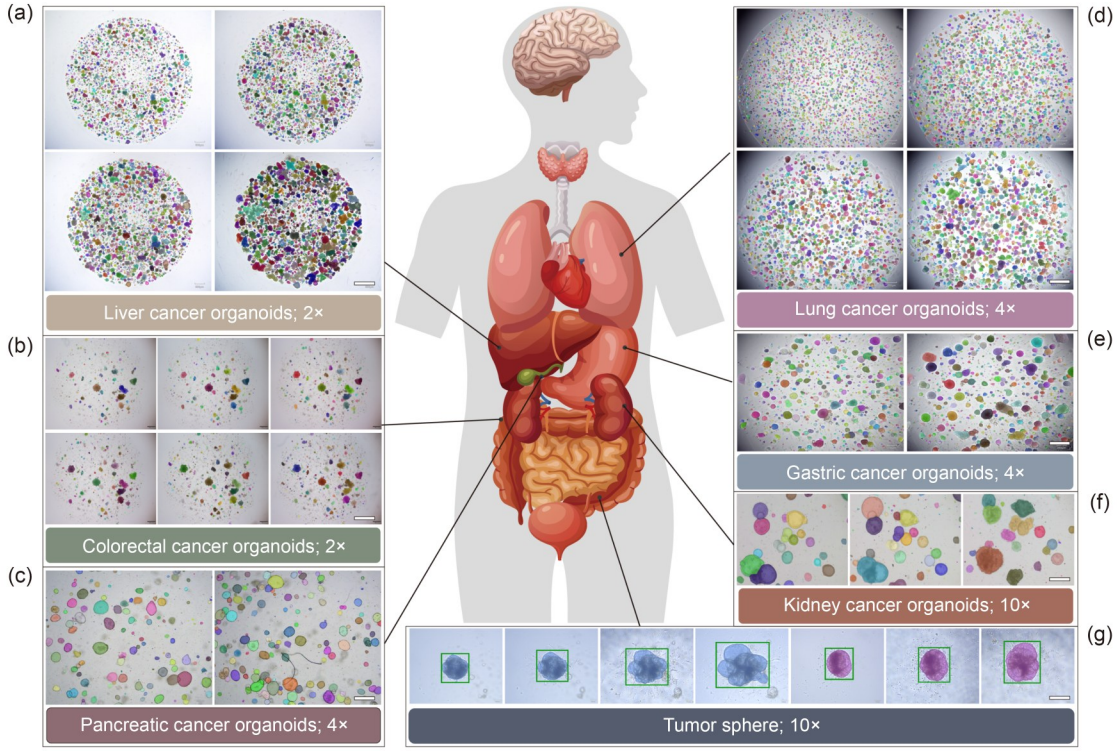

Fig. 1 Segmentation of various organoids in a bright-field image. Different colors indicate individual organoids. (a) Time-lapse segmentation of liver cancer organoids at 2× magnification (scale bar: 1 mm). (b) Time-lapse segmentation of colorectal cancer organoids at 2× magnification (scale bar: 1 mm). (c) Segmentation of pancreatic cancer organoids in different fields of view at 4× magnification (scale bar: 500 μm). (d) Time-lapse segmentation of lung cancer organoids at 4× magnification (scale bar: 500 μm). (e) Time-lapse segmentation of gastric cancer organoids at 4× magnification (scale bar: 500 μm). (f) Time-lapse segmentation of kidney cancer organoids at 10× magnification (scale bar: 200 μm). (g) Time-lapse segmentation of the interaction between two tumor spheres at 10× magnification (scale bar: 200 μm)

address the limitations of traditional segmentation models and comprises four key components. First, the image encoder leverages a visual transformation (ViT) component to encode the input image into a latent feature embedding. Second, the automatic prompt generator generates precise location information for each organoid in the image, which is an essential input for downstream segmentation. Third, the prompt encoder generates sparse prompt embeddings for points or boxes or dense prompt embeddings for masks, depending on the input type. This flexibility allows POST to be applied to different targets. Finally, the mask decoder integrates the image and prompt encoder embeddings to output a multichannel prediction mask. Given the high computational load of SAM when applied to organoid segmentation, we employed a distilled version with a higher processing speed called TinySAM for the mask decoder, and fine-tuned it on organoid and cell datasets to improve the segmentation accuracy [20, 23].

The automatic prompt generator (Fig. 2b) combines object detection with an algorithm we developed called slice-assisted inference that offers a generalizable pipeline for detecting dense and small targets. Various object detection models based on anchor boxes can be used as the organoid detector, such as you only look once (YOLO) [24]. Slice-assisted inference divides the original image into six or more smaller tiles with local overlap, which allows the organoid detector to focus on local regions. To prevent the loss of larger organoids due to the slicing process, global inference is performed on the entire image. Slice-assisted inference maintains efficient memory utilization during processing and can effectively meet the needs of high-resolution image analysis without increasing the size of the model. Because the organoid detector detects multiple slices and the global image, many overlapping bounding boxes are inevitably generated. To address this issue, the automatic prompt generator employs non-maximum suppression based on distance intersection over union (DIoU-NMS) as a filter, which is particularly suitable for occluded and overlapping organoids [25]. During organoid segmentation, bubbles and other impurities in the images can greatly affect the detection accuracy. To address this issue, we collected many organoid images containing bubbles, added them to the training set, and trained the organoid detector to distinguish between bubbles and organoids. To improve the robustness of the organoid recognition performance, multiple data augmentation operations (e.g., geometric transformation and color transformation) were added to the automatic prompt generator. If the organoid detector identifies a

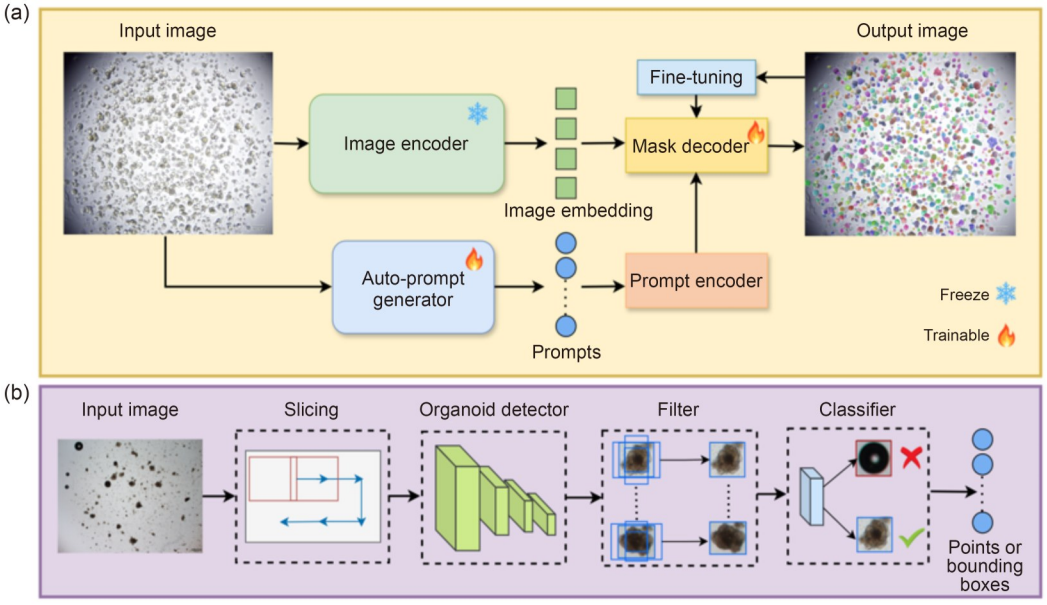

Fig. 2 Algorithm architecture and execution flow. (a) Framework of POST for segmenting any organoid in a bright-field image. The image is initially input into a frozen and parameterized image encoder to generate image embeddings efficiently. Meanwhile, the image is processed by the automatic prompt generator to generate prompt information, which is then processed by the prompt encoder to obtain prompt embeddings. Finally, both the image and prompt embeddings are input into the mask decoder to generate the final segmentation result. (b) Architecture of the automatic prompt generator. The input image is sliced and scaled, and then input into the organoid detector. The organoid detector merges detection boxes and filters impurities to output the center-point coordinates or bounding boxes of detected organoids

target as a bubble, the result is discarded. Finally, precise organoid bounding boxes are extracted and encoded as box or point prompts, which are passed to the mask decoder for subsequent segmentation.

2.2 Performance comparison

We evaluated the performance of POST by conducting comparative experiments on two publicly available cell segmentation datasets: MoNuSeg [26] and the 2018 Data Science Bowl (DSB) [27]. The MoNuSeg dataset was designed for nucleus segmentation and comprises 44 digital microscopic tissue images, of which 30 are training images and 14 are test images. The DSB dataset was designed for nucleus detection in diverse images and contains 670 images, of which 620 are training and validation images, and 50 are test images. In addition, we collected an organoid segmentation dataset containing 1362 bright-field images with approximately 388,000 organoids. The images in this dataset were randomly divided into 80% for training, 10% for validation, and 10% for testing.

POST was trained and compared with several other trained state-of-the-art instance and semantic segmentation models, including Stardist [28], Cellpose [29], U-Net [30], and SAM [20] (Fig. 3a). For consistency and fairness, we adopted the same experimental settings and segmentation parameters as those used in Refs. [20, 28–30]. For the test images, we compared the model predictions with the ground-truth masks at different matching accuracy thresholds based on the standard cross-linking metric (intersection over union (IoU)). The segmentation performance was evaluated by using the F1-score [30, 31]. For nucleus segmentation of the MoNuSeg dataset, Cellpose achieved the highest F1-score while POST performed second-best (Fig. 3b). For nucleus segmentation of the DSB dataset (Fig. 3c), POST performed the best although the differences among POST, Cellpose, and Stardist were marginal. In contrast, POST achieved the best overall organoid segmentation performance when applied to the third dataset of organoid images (Figs. 3d and 3e). Stardist had difficulty in segmenting irregularly shaped, occluded, and overlapping organoids. Meanwhile, Cellpose utilizes a diameter parameter that cannot cover the sizes of all organoids, which makes it easy for this algorithm to misidentify larger or smaller organoids. U-Net and SAM did not perform well on all three datasets. The poor performance of U-Net was attributed to its difficulty with distinguishing individual nuclei or organoids, which is a common limitation of semantic segmentation networks. SAM demonstrated poor generalization for both the nucleus and organoid segmentation tasks.

2.3 Elimination of imaging challenges

While traditional cell images have stable and single morphological characteristics, bright-field images of organoids

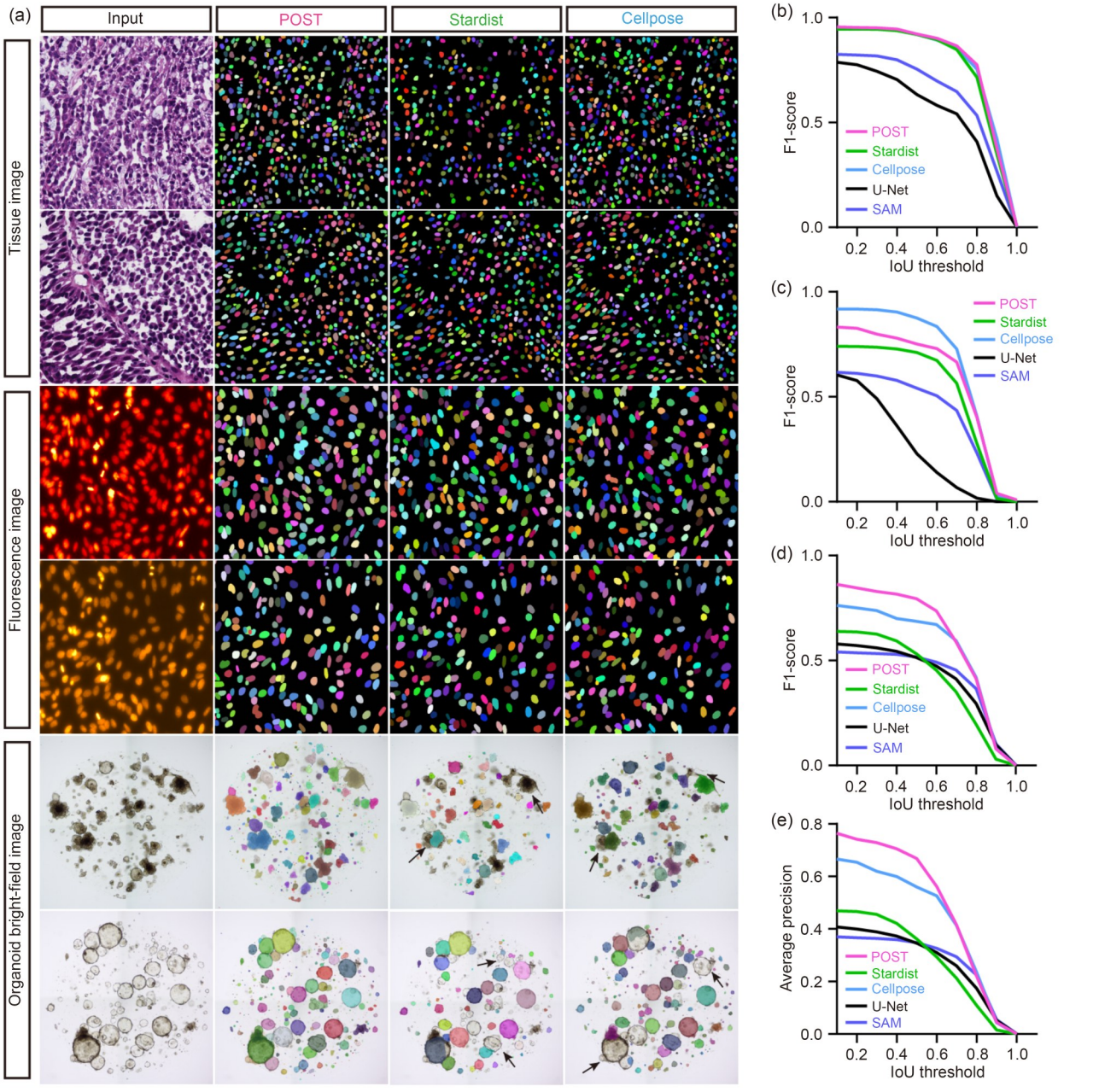

Fig. 3 Segmentation performance of different models (POST, Cellpose, Stardist, U-Net, and SAM) applied to three datasets (MoNuSeg, DSB, and organoid images). Intersection over union (IoU) was used to quantify the match between the predicted and actual masks, where 1.0 means a perfect pixel match and 0.5 means that the number of correctly matched pixels is the same as the number of missing and false positive pixels. The average precision score was calculated by integrating the precision-recall curve and was used to evaluate the segmentation performance. The F1-score combines precision and recall, and was used to measure the model's performance at the pixel level. (a) Segmentation images of models. (b) Nucleus segmentation performance for the MoNuSeg dataset. (c) Nucleus segmentation performance for the DSB dataset. (d, e) Organoid segmentation performance for the bright-field image dataset

are affected by various factors such as the culture environment, imaging conditions, drug effects, and external lighting. Therefore, images obtained under different conditions and at different magnifications will have many artifacts, such as organoid occlusion and overlap, out-of-focus organoids, huge morphological differences, bad lighting conditions, drug effects, dense distribution, sparse distribution, and impurity interference that are difficult for traditional image processing techniques and current artificial intelligence algorithms to handle [11]. We applied POST to various difficult images and used the average precision metric (AP) to evaluate the performance (Fig. 4). POST achieved AP values of 0.81 in the case of severe organoid occlusion and overlap (Fig. 4a), 0.78 in the case of out-of-focus organoids

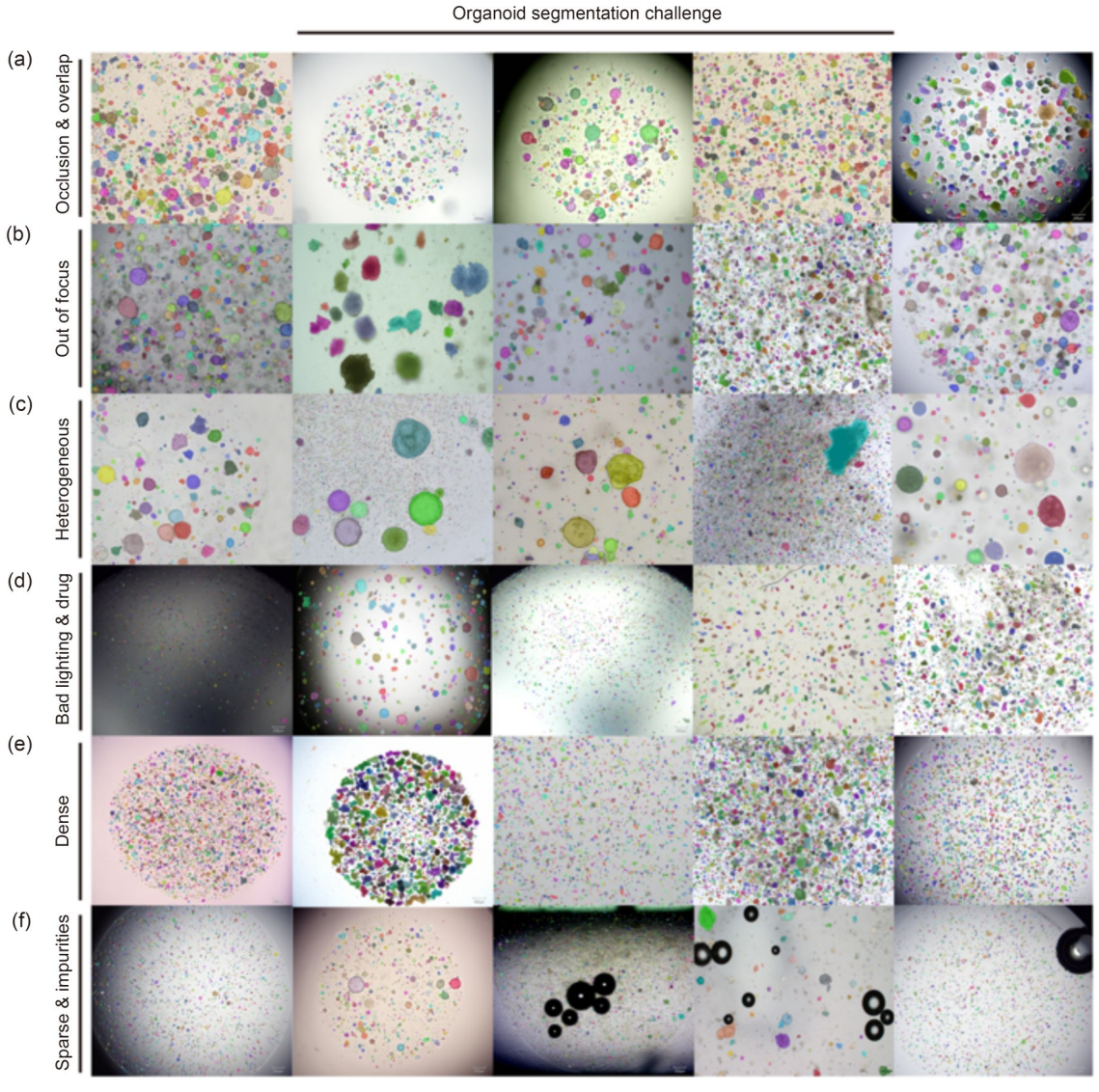

Fig. 4 Performance of POST against various organoid imaging challenges: (a) organoid overlap and occlusion; (b) out-of-focus organoids; (c) nonuniform size distribution; (d) light source and drug effects; (e) overcrowding; (f) sparse distribution and impurity interference

(Fig. 4b), 0.86 in the case of organoids of different sizes (Fig. 4c), 0.83 in the case of poor light sources or drug effects (Fig. 4d), 0.87 in the case of dense organoids (Fig. 4e), and 0.89 in the case of sparse organoids and bubble interference (Fig. 4f). Owing to slice-assisted inference, POST was most accurate at identifying organoids of different sizes and with dense or sparse distributions. POST overcomes organoid overlap and occlusion by accurate boundary delineation. It corrects out-of-focus artifacts by using robust feature detection. It accommodates a nonuniform size distribution for reliable segmentation of different-sized organoids. It resolves overcrowding through precise location. It counteracts light source influence and drug effects by data enhancement. It handles sparse distribution and impurity interference by utilizing slice-assisted inference and training on a large number of noisy samples.

2.4 Drug screening of pancreatic cancer organoids

Anticancer and chemotherapeutic drugs work by preventing the growth and division of cancer cells. We used POST to evaluate the effects of different clinically approved single/combination doses of chemotherapeutic drugs on the growth rate of pancreatic cancer organoids. Pancreatic cancer organoids were thawed and embedded in a 96-well plate matrix for 5 d. Five single-dose or combined-dose chemotherapeutic drug regimens were applied: (1) 1 μmol/L gemcitabine; (2) 2.7 μmol/L erlotinib; (3) 5 μmol/L regorafenib; (4) 1 μmol/L gemcitabine+2.3 μmol/L 5-fluorouracil (5-FU); (5) 1 μmol/L gemcitabine+2.7 μmol/L erlotinib (Fig. 5a). Images of each well were captured in a z-stack by an optical microscope at 4× magnification and a distance of 5 μm

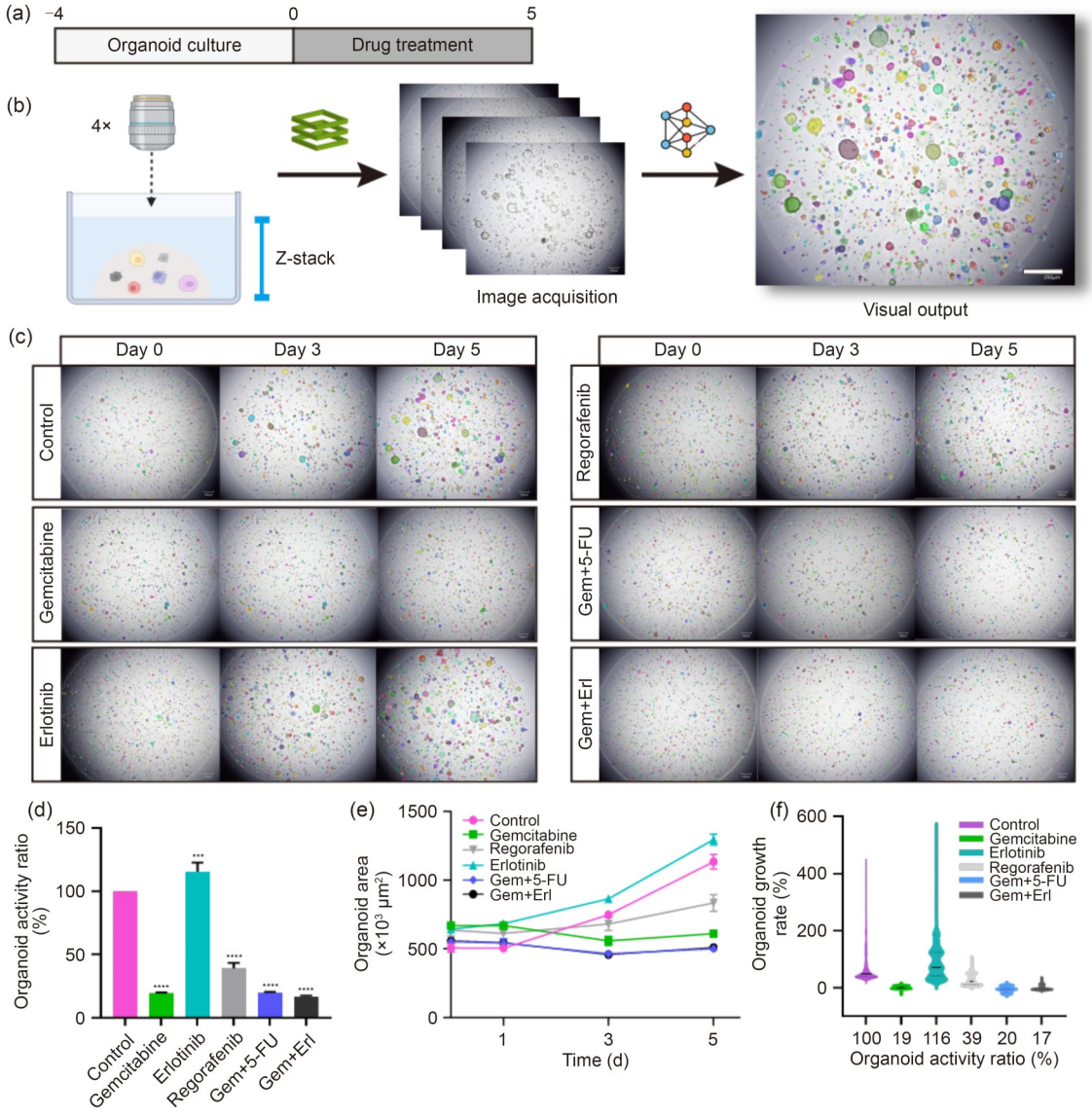

Fig. 5 Application of POST to the automated analysis of anticancer drugs for their efficacy against pancreatic cancer organoids. (a) Organoid culture and treatment schedule. (b) Image acquisition and analysis (scale bar: 500 μm). (c) Segmentation results for the control group and drug-treated groups (Gemcitabine, Erlotinib, Regorafenib, Gemcitabine+5-FU, and Gemcitabine+Erlotinib) (n=3 for each group) on Days 0, 3, and 5. (d) Organoid viability test results of the control and drug-treated groups (n=3). (e) Changes in the overall organoid growth of different groups over time (i.e., area on Day x−area on Day 0; n=3). (f) Organoid growth rates (i.e., (area on Day x−area on Day 0)/area on Day 0×100%) and activities of each group. Each group contained approximately 1500 organoids. In the violin plot, the median is indicated by the center line, and the upper and lower quartiles are indicated by dashed lines. Data in (d, e) are expressed as mean±standard deviation. $^{***}p<0.001$ and $^{****}p<0.0001$

(Fig. 5b). POST was then applied to automatically identify and segment each organoid (Fig. 5c). The segmentation results were then compared with the organoid viability results (Fig. 5d). The growth rates (Fig. 5e) indicated that the Erlotinib group grew better than the control group. While the Regorafenib group also grew, it was greatly inhibited compared with the control group. The Gemcitabine, Gemcitabine+5-FU, and Gemcitabine+Erlotinib groups showed substantial reductions in the organoid growth rate, and the organoids even gradually shrank. The organoid growth rates of each group were then compared with the organoid activity (Fig. 5f) and showed a strong correlation. While the organoid viability test could only measure the whole well, POST could analyze each organoid and obtain the drug resistance performance of different organoids in the same well. For example, although the Erlotinib group demonstrated higher activity and faster growth than the control group, approximately 1/4 of the organoids did not show any growth advantages compared with the control group. In the Regorafenib group, although all organoids were growing, only some organoids showed a growth advantage compared with the control group. In

other groups, most organoids were broken and shrank, and only a few were growing. These results showed that POST could be used to quantify morphological characteristics of each organoid such as the growth rate, which in turn could be used to infer the activity levels of organoids in different groups.

The organoid growth rate was found to follow a mathematical distribution with a mode interval of 20–30 μm (Fig. 6). The efficacy of each drug affected the peak value, steepness, and flatness of the distribution. POST was applied to quantify the morphological characteristics of the organoids including the size distribution. As organoids increased in size, they decreased in number. The organoid size distribution did not change much after the application of a drug. Some organoids grew slowly; others began to shrink; most simply stopped growing. The higher activity of the Erlotinib group compared with the control group was reflected by a larger reduction of organoids in the size range of 10–40 μm and the increase in the number of organoids with a size of 40–200 μm. Compared with the control group, the drugs reduced the number of organoids in the size range of 10–40 μm and increased the number of organoids in the size range of 40–50 μm.

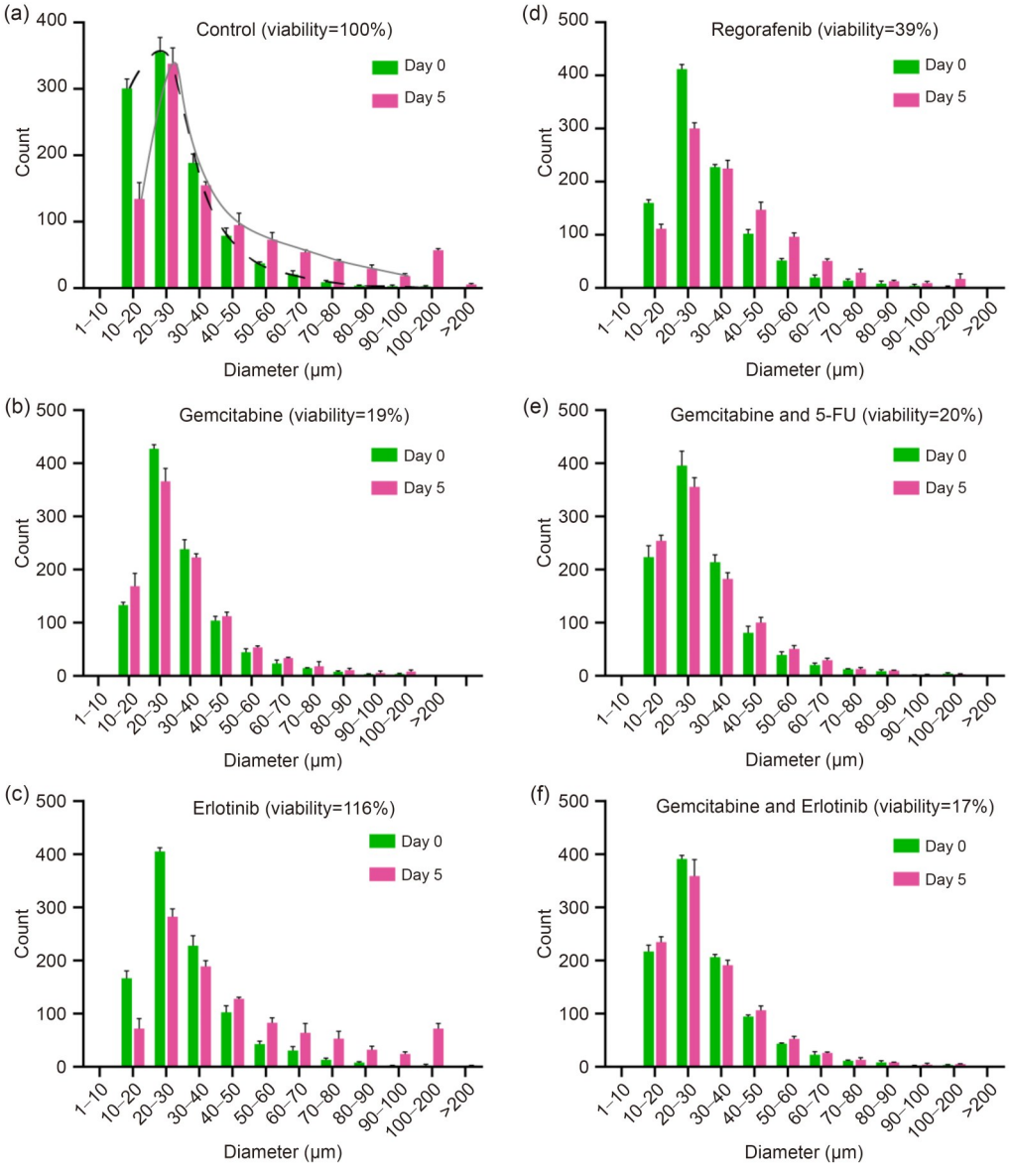

Fig. 6 Size distributions of pancreatic cancer organoids in control and drug-treated groups on Days 0 and 5: (a) control; (b) Gemcitabine; (c) Erlotinib; (d) Regorafenib; (e) Gemcitabine+5-FU; (f) Gemcitabine+Erlotinib. One thousand organoids were randomly selected from each group for analysis (n=3). Data are expressed as mean±standard deviation. Organoids with sizes of 1–100 μm were divided into 10 intervals (10 μm belongs to the 1–10 μm group; 20 μm belongs to the 10–20 μm group; similar for the other groups), and organoids with sizes of 100–200 μm and >200 μm were each placed into additional stages. For each group, the largest number of organoids was in the 20–30 μm stage (i.e., mode interval)

2.5 Drug screening of lung cancer organoids

Next, we applied POST to evaluate the effects of anticancer drugs on the morphology of lung cancer organoids that were thawed and embedded in a 96-well plate matrix for 7 d. Five chemotherapy drug regimens were applied at concentrations of 2 or 10 μmol/L on Day 0 (Fig. 7a). Images of each well were captured by an optical microscope at 10× magnification and a distance of 25 μm (Fig. 7b). POST was able to accurately identify and segment single/multiple

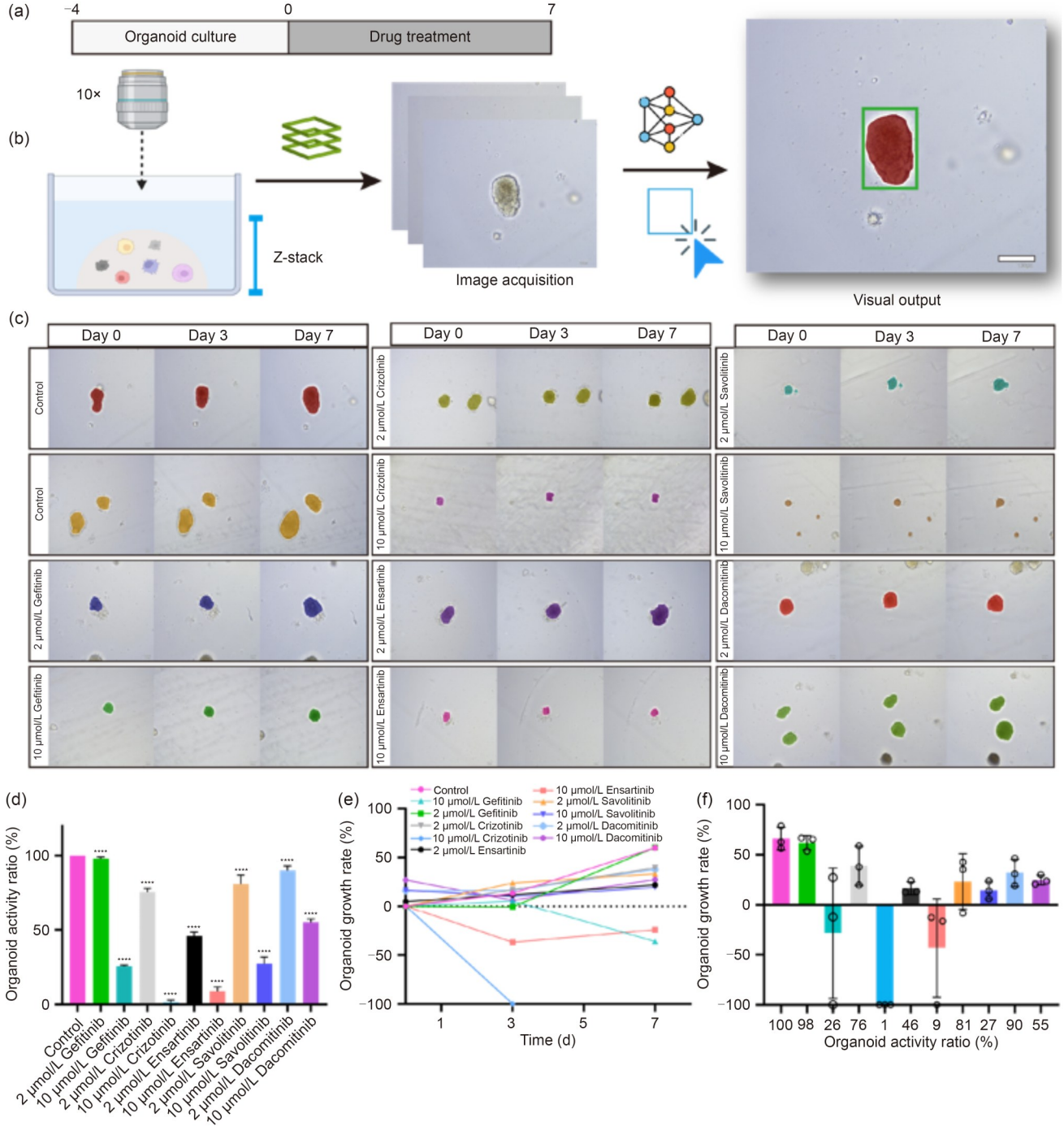

Fig. 7 Application of POST to the automated analysis of anticancer drugs for their efficacy against lung cancer organoids. (a) Organoid culture and drug treatment schedule. (b) Image acquisition and analysis (scale bar: 200 μm). (c) Segmentation results for the control group and 10 drug-treated groups (concentrations of 2 and 10 μmol/L, n=3) on Days 0, 3, and 7. (d) Viability results of the control and drug-treated groups (n=3). (e) Changes in the overall growth rates of different drug-treated groups over time (i.e., (area on Day x−area on Day 0)/area on Day 0×100%). (f) Organoid growth rate and organoid activity of each group (3–5 organoids for each group). Data in (d–f) are expressed as mean±standard deviation. $^{****}p<0.0001$

organoids in the control and drug-treated groups (Fig. 7c). Corresponding organoid viability experiments were performed to verify the morphological analysis (Fig. 7d). The growth rates of the different groups were compared (Fig. 7e). Most organoids in the drug-treated groups were able to grow but were inhibited to varying degrees compared with organoids in the control group. A low concentration of gefitinib inhibited growth on Day 3, but the growth rate was close to that of the control group by Day 7. At high concentrations, some drugs caused organoids to shrink or even die. The growth rates of each group were then compared with the organoid activity (Fig. 7f), which generally showed a strong correlation. However, not all growth rates were consistent with organoid activity. For example, a low concentration of savolitinib resulted in a relatively high growth rate, but there were still cases of organoid lysis and shrinkage. Organoids treated with a low concentration of dacomitinib exhibited a significantly lower growth rate than those treated with a high concentration. These differences in the response of individual organoids to anticancer drugs reflect the complexity and heterogeneity of cancer. POST could identify the heterogeneity of individual organoids in their drug tolerance, which is promising for studying the specificity of tumors. Because POST can accurately segment each organoid, it can be used to analyze the various morphological characteristics of the organoids that change over time, including the circumference, diameter, roundness, eccentricity, Euler number, aspect ratio, multiscale entropy, and redundant circumference. Thus, it can be used to analyze the morphology of organoids from different angles.

3 Discussion

POST is a generalized model specifically designed for organoid segmentation. Compared with other models, it can accurately and quickly segment multiple types of organoids in a single image without parameter tuning. It has three major innovations:

(1) It combines slice-assisted inference with a mainstream object detection model and incorporates filtering and classification modules to effectively address various challenges in organoid imaging.

(2) It adopts the efficient and lightweight TinySAM and is trained on cell and organoid datasets for enhanced generalization ability.

(3) It can achieve fast and efficient interactive segmentation of any organoid and cell, and can be adapted to devices with only a central processing unit (CPU).

Segmentation experiments on three datasets demonstrated the effectiveness and generalization ability of POST. Drug screening experiments confirmed that the model's results were strongly consistent with the results of viability tests. While viability tests can only evaluate the effects of a drug on the entire well, POST can quantify morphological changes in individual organoids within the well, which facilitates accurate quantification of the drug's efficacy on organoids of different sizes [32]. Not all organoids in a well have a growth rate that is consistent with the viability test results. Thus, POST is particularly useful for continuously tracking the heterogeneous changes of individual organoids [33]. Compared to fully automated segmentation algorithms, POST allows for segmentation guided by manual prompts, which offers greater flexibility and effectively mitigates issues such as erroneous segmentation or omission of organoids [14, 15, 22].

One promising direction for POST is the evaluation of external stimuli for various tumor organoids. Mechanical, optical, and electrical stimuli can greatly affect the morphology and behavior of cells, such as their proliferation, differentiation, and survival. Therefore, determining the optimal type, intensity, and duration of these stimuli for building organoids is critical. Traditional analysis methods are inefficient and time-consuming, and cannot handle large-scale data. Therefore, POST can provide a more accurate and convenient way to identify and quantify these stimuli in organoid studies. Another promising direction for POST is the coculturing of cells and organoids. Simulating the complex cellular environment in vivo can help with studying cell interactions, such as immune cells killing tumor cells. POST can help with accurately segmenting different cell types by generating different prompts for cell classes. It can help researchers understand biological processes more deeply, explore new treatments, and promote the progress of biomedical research by analyzing cell and organoid cocultures. Finally, POST can be used for individualized tumor organoid analysis. Understanding tumor heterogeneity is crucial for studying basic cancer biology and developing new treatment strategies. Even in the same batch of tumors, individual tumors may have different genetic mutations that can affect the mechanism of a drug. Individual organoids may also have different gene expression patterns, which affect the accessibility of drug targets and, in turn, drug efficacy. POST can facilitate the development of personalized medicine and the analysis of tumor heterogeneity. While we focused on bright-field imaging analysis, we may need to incorporate multiscale analysis, including 3D fluorescence imaging, so the applicability of POST to multiple imaging methodologies should be considered in future research.

4 Conclusions

POST is an accurate and robust organoid segmentation model that surpasses existing algorithms. It effectively addresses the challenges encountered during organoid imaging

and cultivation to facilitate the precise extraction of morphological features from individual organoids. Notably, it incorporates both automatic and interactive segmentation, with the latter serving as a complementary tool to the former. This dual approach helps mitigate inaccuracies in automated segmentation and reduce potential errors. POST can improve the efficiency and quality of drug screening tests using tumor organoids and provide a valuable complement to cell viability assays in complex experimental settings. Although the results presented here are promising, several issues still require further exploration and development. More drug screening experiments are needed to improve the robustness and reliability of POST. We believe that POST may accelerate the transition of organoid models from laboratory research to clinical applications, advance the precision and commercialization of organoid technology, and establish it as a vital tool for drug development and biomedical research.

5 Materials and methods

5.1 Image acquisition

We used an Avatarget high-content organoid imaging and analysis device to collect images for the organoid segmentation dataset. In normal bright-field mode, images of organoids suspended in hydrogel for different days were obtained under 2×, 4×, 10×, and 20× magnifications. These images included various tumor organoids, including colorectal cancer, pancreatic cancer, lung cancer, gastric cancer, kidney cancer, liver cancer, prostate cancer, ovarian cancer, and tumor spheres. Some images were converted into high-throughput images by synthesizing z-stack images using a focus-stacking algorithm, which allowed all organoids to be imaged. In addition, some organoid images were stitched to obtain a larger field of view. The image sizes were either 2248×2048 or 1360×1024 pixels, and the images were saved in JPG format.

5.2 Data annotation

Each image in the organoid segmentation dataset was manually annotated by two experienced experts using the LabelMe software. The consistency was calculated according to the IoU; if the score was less than 80%, the image was further annotated by a third expert. The labels contained the identities and masks of different organoid instances. For each organoid instance, we assigned a unique numerical identity (ID) (starting from 1) that corresponded to the pixel value of the organoid. IDs could not repeat within the same label but may appear in multiple labels. In the organoid segmentation dataset, bounding boxes were automatically generated from the labeled masks by use of automated scripts with a small number of bubble images added. Each image was labeled and checked for consistency by experts using the labelImg software to distinguish organoids and bubbles into separate categories.

5.3 Image encoder

SAM is a large transformer model trained on the SA-1B dataset, which is a large visual corpus with over 1 billion masks on 11 million licensed and privacy-respecting images. It was designed and trained to perform zero-shot transfer to new image distributions and tasks, achieving results comparable to those of fully supervised trained models. However, despite the versatility and success of SAM in general image segmentation, its application to organoids still has certain limitations. First, although SAM includes a complex and efficient data engine, it was trained on only a relatively small number of biomedical images [34]. Therefore, SAM often does not produce the correct results when applied directly to segmenting organoids. Second, the huge computational costs of SAM have limited its practical application [23].

SAM comprises three sub-networks: an image encoder, a hint encoder, and a mask decoder. The image encoder, which is based on ViT, is computationally expensive. Inspired by MobileSAM [35], we replaced the original image encoder with the lightweight TinyViT [36], but this substitution led to substantial performance degradation. To address this, we adopted a knowledge distillation strategy to guide the learning of the lightweight image encoder across multiple knowledge levels. Specifically, we selected the intermediate layers of the teacher network to guide the student network. The output of the image encoder (i.e., image embedding) was used as the distilled information encapsulating the essential features of the input image for the prediction process.

For an input image I, the distillation loss for the image embedding is defined as

$$\mathcal{L}_{\text{embedding}} = D\left(E_{\text{T}}^{\text{img}}, E_{\text{S}}^{\text{img}}\right), \tag{1}$$

where $E_{\text{S}}^{\text{img}}$ and $E_{\text{T}}^{\text{img}}$ represent the encoders of the student and teacher networks, respectively. Because image-level information is less directly related to mask prediction, features closer to the final output are more critical for segmentation tasks. The final output of the teacher network is selected as the distillation point. The output distillation loss $\mathcal{L}_{\text{output}}$ can be defined as

$$\mathcal{L}_{\text{output}} = \mathcal{L}\left(M_{\text{T}}^{\text{d}}\left(E_{\text{T}}^{\text{img}}(I), q\right), M_{\text{S}}^{\text{d}}\left(E_{\text{S}}^{\text{img}}(I), q\right)\right), \tag{2}$$

where M_{S}^{d} and M_{T}^{d} represent the mask decoders of the student and teacher networks, respectively. Here, q denotes the query of the mask decoder, which is the concatenation of the prompt embedding and output tokens.

5.4 Fine-tuning

We leveraged the ability of TinySAM to bundle and process multiple cues per image to fine-tune its performance when applied to biological images. The SAM family of models supports three segmentation modes: automatic segmentation, cued segmentation using points, and cued segmentation using bounding boxes. Previous studies on applying SAM to image segmentation have shown that the bounding box method is the most effective and accurate for describing complex structures in biomedical images [21, 22]. We fine-tuned TinySAM by combining the bounding box cues from multiple ground-truth masks in the same image. By incorporating the positional encoding of multiple regions of interest when generating segmentation masks, we effectively addressed the inherent complexity of organoid images to alleviate cue ambiguity and improve segmentation accuracy. Parameter-efficient fine-tuning (PEFT) is an effective refinement method for large models, where a small portion of the model parameters are selectively updated to improve their generalization ability for a specific task and prevent the model from collapsing. Therefore, we froze the image encoder of TinySAM to generate image embeddings before training to reduce the computational burden [22]. We then trained the mask decoder and calculated the loss $\mathcal{L}_{\text{Total}}$ in each epoch by obtaining the weighted sum of the Dice loss and cross-entropy loss, which is a robust approach for segmentation tasks [22, 37]. The Dice loss $\mathcal{L}_{\text{Soft-Dice}}$ is calculated as follows:

$$\mathcal{L}_{\text{Soft-Dice}}=1-\frac{2\sum\left(y\cdot\hat{y}\right)}{\sum y+\sum\hat{y}}, \tag{3}$$

where y and $\hat{y}$ are the target and predicted values, respectively, and are usually binary labels or probability maps. The performance was further improved by assigning weights to different categories (foreground and background). The cross-entropy loss $\mathcal{L}_{\text{BCE}}$ is calculated as follows:

$$\mathcal{L}_{\text{BCE}}=\sum\nolimits_{c} y_c \ln\left(p_c\right), \tag{4}$$

where y_c is the true label (one-hot encoding) and p_c is the predicted class probability. This is a standard classification loss function that calculates the difference between the predicted probability and the actual label for each pixel. Finally, $\mathcal{L}_{\text{Total}}$ is obtained by adding $\mathcal{L}_{\text{BCE}}$ and $\mathcal{L}_{\text{Soft-Dice}}$:

$$\mathcal{L}_{\text{Total}}=\mathcal{L}_{\text{BCE}}+\mathcal{L}_{\text{Soft-Dice}}. \tag{5}$$

5.5 Image slicing

In organoid segmentation, the detection of very small and densely distributed organoids is a major challenge. Very small organs can be represented by only a few pixels. Meanwhile, densely distributed organoids are heavily occluded and lack sufficient details [38, 39]. To overcome these problems, bright-field images can be augmented by the extraction of patches. Each input image (F_1, F_2, ⋯) can be sliced into overlapping patches (P_1, P_2, ⋯), where the patch dimension, number of slices, and overlap ratio are all used as hyperparameters (Fig. S2a in the supplementary information). As the patch size decreases, larger organoids may not fit into the slices and intersection regions, which may impact the detection of large organoids. For slice-assisted inference (Fig. S2b in the supplementary information), the input image F was sliced into $M\times N$ overlapping patches (P_1, P_2, ⋯, P_{MN}). Then, the size of each patch was resized while the aspect ratio was maintained. The organoid detector then performed global inference on the original image to detect larger organoids across all patches.

5.6 Organoid detector

POST utilized various object detection models as the organoid detector. In this study, we selected YOLOv9 as the organoid detector owing to its accuracy and speed [24]. Traditional deep neural networks suffer from large amounts of information loss when performing feature extraction and spatial transformation layer by layer. YOLOv9 overcomes this problem by building on the success of previous YOLO versions and introducing innovative technologies such as programmable gradient information and general and efficient layer aggregation networks. It has excellent accuracy for target detection tasks, and its highly optimized network structure gives it fast reasoning capabilities. It performs particularly well in detecting complex scenes and small targets. Because YOLOv9 is an anchor-free target detection algorithm, it does not require predefined anchor frames. It is not restricted by the size or aspect ratio of anchor boxes, so it is better suited for detecting various organoids that exhibit large variations in morphology and size.

5.7 Organoid filtering and sorting

The organoid detector extracts bounded boxes from multiple image slices and a global image, which often leads to a significant number of overlapping boxes. Traditional non-maximum suppression (NMS) tends to discard overlapping candidate boxes, which increases the missed detection of organoids [40]. In contrast, DIoU-NMS considers not only IoU but also the distance between the candidate box and the center point of the box with the maximum score:

$$\text{DIoU}=\text{IoU}-\frac{\rho^2\left(b,b_{\text{gt}}\right)}{c_{\text{m}}^2}. \tag{6}$$

Because of the distance penalty, the area where the center of the target is far away is not easily merged by error. $\rho(b,b_{\text{gt}})$ is the Euclidean distance between the center points of box b and box b_{gt}. Parameter c_{m} is the maximum

diagonal length, which makes sure that DIoU has a value between 0 and 1. A classifier is then used to determine whether the detected target represents an organoid or other impurities (e.g., bubble, hydrogel), and only the bounding boxes of organoids are retained. Finally, the bounding box is encoded to generate a box or point prompt.

5.8 Prompt-guided interactive segmentation

TinySAM is an advanced segmentation algorithm that can create segmentation masks using different hints such as point, box, and mask prompts. We fine-tuned the model on organoid and cell datasets to accelerate its feature extraction process so that it can quickly and interactively segment various organoids and cells. We simulated this use case by manually placing points or box hints in the target organoid area to obtain prediction results. We achieved accurate results by testing organoid and cell segmentation in various imaging modes (Fig. S3 in the supplementary information).

5.9 Evaluation metrics

We quantified the prediction performance of POST by matching each predicted mask to the most similar ground-truth mask, which was defined by the IoU. The F1-score and AP for each image were defined by using true positives (TP, i.e., predicted masks having an IoU with the ground-truth mask at or above a given threshold), false positives (FP, no matching predicted masks), and false negatives (FN, no matching ground-truth masks). The above metrics were calculated as follows:

$$\mathrm{AP}=\frac{\mathrm{TP}}{\mathrm{TP}+\mathrm{FP}+\mathrm{FN}}, \tag{7}$$

$$\mathrm{Precision}=\frac{\mathrm{TP}}{\mathrm{TP}+\mathrm{FP}}, \tag{8}$$

$$\mathrm{Recall}=\frac{\mathrm{TP}}{\mathrm{TP}+\mathrm{FN}}, \tag{9}$$

$$\text{F1-score}=2\times\frac{\mathrm{Precision}\times\mathrm{Recall}}{\mathrm{Precision}+\mathrm{Recall}}. \tag{10}$$

5.10 Hardware specifications

A computer with the following specifications was used: central processing unit (CPU): Intel Xeon Gold 6348; motherboard: Z390 UD; RAM: 32 GB (DDR4, 2666 MHz); hard disk: 500 GB 860 EVO SSD; graphics card: 4× NVIDIA GeForce RTX 2080 Ti (11 GB); system: Ubuntu 22.04 LTS (Jammy Jellyfish).

Supplementary Information The online version contains supplementary material available at https://doi.org/10.1631/bdm.2500119.

Acknowledgements This work was supported by the National Key R&D Program of China (No. 2022YFC2504403), the National Natural Science Foundation of China (No. 62172202), the Experiment Project of China Manned Space Program (No. HYZHXM01019), and the Fundamental Research Funds for the Central Universities from Southeast University (No. 3207032101C3).

Author contributions XD, ZZC, and YHL were involved in conceptualization; XD and JPS contributed to formal analysis; ZZC and ZZG were involved in funding acquisition; XD helped in the investigation; JZ helped in drug testing. XD, YCL, ZLZ, and JPS contributed to image annotation; YHL and ZZG were involved in project administration; ZZC and YHL helped in supervision; XD, JPS, and YCL contributed to validation; XD, ZZC, and YHL were involved in writing the original draft; XD, YCL, ZZC, and YHL helped in writing—review & editing.

Declarations

Conflict of interest ZZG is an editorial board member for *Bio-Design and Manufacturing* (*BDM*). ZZC is a guest editor of the Special Column on AI-Powered Biofabrication of *BDM*. They were not involved in the editorial review or the decision to publish this article. The authors declare that they have no known competing financial interests or personal relationships that could have appeared to influence the work reported in this paper.

Ethical approval Patient-derived organoids were established and utilized in this study under the approval of the Institutional Ethics Committee (Approval Nos. 2022-SR-624 and 2024-206-02). All experimental procedures involving human samples were performed in compliance with relevant ethical regulations.

Data availability All data required to evaluate the conclusions of the paper have been provided in the paper and/or supplementary information. Additional data related to this paper may be requested from the authors. The custom code can be available in the public GitHub repository at https://github.com/duxuan11/Precision-Organoid-Segmentation-Technique-POST.git. The dataset can be downloaded from https://drive.google.com/file/d/1bhC6oBYq8czaa2YyQBQLtzqfhIIHVe_q/view?usp=sharing.

References

1. Heydari Z, Moeinvaziri F, Agarwal T et al (2021) Organoids: a novel modality in disease modeling. Bio-Des Manuf 4(4):689–716. https://doi.org/10.1007/s42242-021-00150-7
2. Sun XX, Yang XH, Chen Y et al (2023) *In situ* self-assembled nanomedicines for cancer treatment. Chem Eng J 466:143365. https://doi.org/10.1016/j.cej.2023.143365
3. Drost J, Clevers H (2018) Organoids in cancer research. Nat Rev Cancer 18(7):407–418. https://doi.org/10.1038/s41568-018-0007-6
4. Yuan J, Li XY, Yu SJ (2023) Cancer organoid co-culture model system: novel approach to guide precision medicine. Front Immunol 13:1061388. https://doi.org/10.3389/fimmu.2022.1061388
5. Zhao H, Yan C, Hu YB et al (2019) Sphere-forming assay vs. organoid culture: determining long-term stemness and the chemoresistant capacity of primary colorectal cancer cells. Int J Oncol 54(3):893–904. https://doi.org/10.3892/ijo.2019.4683
6. Bian XS, Li G, Wang C et al (2021) OrgaNet: a deep learning approach for automated evaluation of organoids viability in drug screening. In: International Symposium on Bioinformatics Research and Applications, p.411–423. https://doi.org/10.1007/978-3-030-91415-8_35

7. Ley-Ngardigal S, Bertolin G (2022) Approaches to monitor ATP levels in living cells: where do we stand? FEBS J 289(24): 7940–7969. https://doi.org/10.1111/febs.16169
8. Cai L, Qin X, Xu Z et al (2019) Comparison of cytotoxicity evaluation of anticancer drugs between real-time cell analysis and CCK-8 method. ACS Omega 4(7):12036–12042. https://doi.org/10.1021/acsomega.9b01142
9. Bian XS, Li G, Wang C et al (2021) A deep learning model for detection and tracking in high-throughput images of organoid. Comput Biol Med 134:104490. https://doi.org/10.1016/j.compbiomed.2021.104490
10. Haja A, Horcas-Nieto JM, Bakker BM et al (2023) Towards automatization of organoid analysis: a deep learning approach to localize and quantify organoid images. Comput Meth Programs Biomed Update 3:100101. https://doi.org/10.1016/j.cmpbup.2023.100101
11. Kassis T, Hernandez-Gordillo V, Langer R et al (2019) OrgaQuant: human intestinal organoid localization and quantification using deep convolutional neural networks. Sci Rep 9:12479. https://doi.org/10.1038/s41598-019-48874-y
12. Du X, Chen ZZ, Li QW et al (2023) Organoids revealed: morphological analysis of the profound next generation in-vitro model with artificial intelligence. Bio-Des Manuf 6(3):319–339. https://doi.org/10.1007/s42242-022-00226-y
13. Gritti N, Lim JL, Anlaş K et al (2021) MOrgAna: accessible quantitative analysis of organoids with machine learning. Development 148(18):dev199611. https://doi.org/10.1242/dev.199611
14. Powell RT, Moussalli MJ, Guo L et al (2022) deepOrganoid: a brightfield cell viability model for screening matrix-embedded organoids. SLAS Discov 27(3):175–184. https://doi.org/10.1016/j.slasd.2022.03.004
15. Matthews JM, Schuster B, Kashaf SS et al (2022) OrganoID: a versatile deep learning platform for tracking and analysis of single-organoid dynamics. PLoS Comput Biol 18(11):e1010584. https://doi.org/10.1371/journal.pcbi.1010584
16. Wang XW, Wu CY, Zhang SD et al (2022) A novel deep learning segmentation model for organoid-based drug screening. Front Pharmacol 13:1080273. https://doi.org/10.3389/fphar.2022.1080273
17. Lefferts JW, Kroes S, Smith MB et al (2024) OrgaSegment: deep-learning based organoid segmentation to quantify CFTR dependent fluid secretion. Commun Biol 7(1):319. https://doi.org/10.1038/s42003-024-05966-4
18. Leng B, Jiang H, Wang BD et al (2024) Deep-Orga: an improved deep learning-based lightweight model for intestinal organoid detection. Comput Biol Med 169:107847. https://doi.org/10.1016/j.compbiomed.2023.107847
19. Chen ZZ, Ma N, Sun XW et al (2021) Automated evaluation of tumor spheroid behavior in 3D culture using deep learning-based recognition. Biomaterials 272:120770. https://doi.org/10.1016/j.biomaterials.2021.120770
20. Kirillov A, Mintun E, Ravi N et al (2023) Segment anything. In: IEEE/CVF International Conference on Computer Vision, p.3992–4003. https://doi.org/10.1109/ICCV51070.2023.00371
21. Huang YH, Yang X, Liu L et al (2024) Segment anything model for medical images? Med Image Anal 92:103061. https://doi.org/10.1016/j.media.2023.103061
22. Ma J, He YT, Li FF et al (2024) Segment anything in medical images. Nat Commun 15:654. https://doi.org/10.1038/s41467-024-44824-z
23. Shu H, Li W, Tang Y et al (2025). TinySAM: pushing the envelope for efficient segment anything model. In: Proceedings of the AAAI Conference on Artificial Intelligence, p.20470–20478. https://doi.org/10.1609/aaai.v39i19.34255
24. Wang CY, Yeh IH, Mark Liao HY (2024) YOLOv9: learning what you want to learn using programmable gradient information. In: European Conference on Computer Vision, p.1–21. https://doi.org/10.1007/978-3-031-72751-1_1
25. Zheng ZH, Wang P, Liu W et al (2020) Distance-IoU loss: faster and better learning for bounding box regression. In: Proceedings of the AAAI Conference on Artificial Intelligence, p.12993–13000. https://doi.org/10.1609/aaai.v34i07.6999
26. Kumar N, Verma R, Sharma S et al (2017) A dataset and a technique for generalized nuclear segmentation for computational pathology. IEEE Trans Med Imag 36(7):1550–1560. https://doi.org/10.1109/TMI.2017.2677499
27. Caicedo JC, Goodman A, Karhohs KW et al (2019) Nucleus segmentation across imaging experiments: the 2018 Data Science Bowl. Nat Methods 16(12):1247–1253. https://doi.org/10.1038/s41592-019-0612-7
28. Schmidt U, Weigert M, Broaddus C et al (2018) Cell detection with star-convex polygons. In: International Conference on Medical Image Computing and Computer-Assisted Intervention, p.265–273. https://doi.org/10.1007/978-3-030-00934-2_30
29. Stringer C, Wang T, Michaelos M et al (2021) Cellpose: a generalist algorithm for cellular segmentation. Nat Methods 18(1): 100–106. https://doi.org/10.1038/s41592-020-01018-x
30. Ronneberger O, Fischer P, Brox T (2015) U-Net: convolutional networks for biomedical image segmentation. In: International Conference on Medical Image Computing and Computer-Assisted Intervention, p.234–241. https://doi.org/10.1007/978-3-319-24574-4_28
31. Long J, Shelhamer E, Darrell T (2015) Fully convolutional networks for semantic segmentation. In: IEEE Conference on Computer Vision and Pattern Recognition, p.3431–3440. https://doi.org/10.1109/CVPR.2015.7298965
32. Vlachogiannis G, Hedayat S, Vatsiou A et al (2018) Patient-derived organoids model treatment response of metastatic gastrointestinal cancers. Science 359(6378):920–926. https://doi.org/10.1126/science.aao2774
33. Kim J, Koo BK, Knoblich JA (2020) Human organoids: model systems for human biology and medicine. Nat Rev Mol Cell Biol 21(10):571–584. https://doi.org/10.1038/s41580-020-0259-3
34. Na S, Guo Y, Jiang F et al (2024) Segment any cell: a SAM-based auto-prompting fine-tuning framework for nuclei segmentation. https://doi.org/10.48550/arXiv.2401.13220
35. Zhang C, Han D, Qiao Y et al (2023) Faster segment anything: towards lightweight SAM for mobile applications. https://doi.org/10.48550/arXiv.2306.14289.
36. Wu K, Zhang JN, Peng HW et al (2022) TinyViT: fast pretraining distillation for small vision transformers. In: European Conference on Computer Vision, p.68–85. https://doi.org/10.1007/978-3-031-19803-8_5
37. Isensee F, Jaeger PF, Kohl SAA et al (2021) nnU-Net: a self-configuring method for deep learning-based biomedical image segmentation. Nat Methods 18(2):203–211. https://doi.org/10.1038/s41592-020-01008-z
38. Chen ZG, Wu KH, Li YB et al (2019) SSD-MSN: an improved multi-scale object detection network based on SSD. IEEE Access 7:80622–80632. https://doi.org/10.1109/ACCESS.2019.2923016
39. Kisantal M, Wojna Z, Murawski J et al (2019) Augmentation for small object detection. https://doi.org/10.48550/arXiv.1902.07296
40. Neubeck A, Van Gool L (2006) Efficient non-maximum suppression. In: 18th International Conference on Pattern Recognition, p.850–855. https://doi.org/10.1109/icpr.2006.479